INORGANIC CHEMISTRY FRONTIERS

RESEARCH ARTICLE

View Article Online
View Journal | View Issue

Cite this: *Inorg. Chem. Front.*, 2025, **12**, 8055

Subgrid cage confinement engineering enabled ultra-efficient near-infrared Cr^{3+}–Ln^{3+} co-doped phosphors

Simeng Cao,[a] Shaoan Zhang, *[a] Ximei An,[a] Lei Yang,[a] Mengting Gao,[a] Zhiyue Yang,[a] Chao He,[a] Zonglong Guo[a] and Yang Li *[a,b]

Precise control of energy migration between Cr^{3+} sensitizers and Ln^{3+} activators at the topochemical subgrid level remains a fundamental challenge. Herein, a novel subgrid cage confinement engineering strategy was proposed, achieving ultra-efficient near-infrared (NIR) Cr^{3+}–Ln^{3+} (Ln = Yb, Nd, Er) co-doped phosphors. The bilayer cage architecture of $GdAl_{1.5}Ga_{1.5}(BO_3)_4$ precisely confines Ln^{3+} at the central Gd^{3+} sites, while providing octahedral lattice positions for Cr^{3+} substitution within the Al/GaO_6 framework. This unique confinement constrains Cr^{3+}–Ln^{3+} separation to the optimal 3.67 Å while increasing the Ln^{3+}–Ln^{3+} distance to 5.92 Å, enabling highly efficient Cr^{3+}–Ln^{3+} energy transfer (η_{ETE}: 61% for Yb^{3+}, 82% for Nd^{3+}, 46% for Er^{3+}) and suppressing energy losses between neighbouring Ln^{3+} ions. Consequently, the Cr^{3+}–Yb^{3+} co-doped system achieved a high photoluminescence quantum yield of 86% and retained 94% of its intensity even at 423 K, demonstrating exceptional thermal stability. The fabricated NIR phosphor-converted light-emitting diodes delivered a NIR output power of 127 mW with a photoelectric efficiency of 13% under a 300 mA operating current. These capabilities enabled high-contrast biological imaging applications, such as vein visualization and non-destructive testing, as validated by prototype demonstrations.

Received 10th July 2025,
Accepted 12th August 2025

DOI: 10.1039/d5qi01468a

rsc.li/frontiers-inorganic

1. Introduction

In near-infrared (NIR) luminescent materials, Cr^{3+}–Ln^{3+} co-doped systems exhibit significant advantages through precise interionic energy transfer and local structural modulation strategies. These systems can extend their emission spectra to an ultra-broad band of 650–1600 nm, fully covering the three characteristic optical transparency windows of biological tissues (Window I: 700–950 nm; Window II: 1000–1350 nm; Window III: 1500–1800 nm).[1,2] Simultaneously, the broadband absorption of Cr^{3+} (300–650 nm) efficiently sensitizes rare-earth ions, significantly enhancing the excitation efficiency of Ln^{3+} (*e.g.*, Yb^{3+}, Nd^{3+}, and Er^{3+}), thereby overcoming the inherent limitation of small absorption cross-sections in conventional rare-earth materials.[3–5] However, the photoluminescence quantum yield (PLQY) of these systems is strictly constrained by the $Cr^{3+} \rightarrow Ln^{3+}$ energy transfer efficiency (η_{ETE}), which is intrinsically linked to ionic lattice occupancy, doping concentration, chemical states, and local crystal field environments.[6,7] Conventional strategies involve screening host lattice sites (*e.g.*, ensuring Cr^{3+} occupies octahedral sites while Ln^{3+} occupies high-coordination dodecahedral sites) and modulating unit cell parameters in solid solutions (*e.g.*, $(Y,Lu)_3(Al,Ga)_5O_{12}$) to optimize the Cr^{3+}–Ln^{3+} separation to the ideal energy transfer distance of 3–6 Å.[8,9] Although these approaches can enhance luminescence efficiency, achieving precise control over energy migration at the topochemical subgrid level remains a fundamental challenge.[10,11]

Addressing this challenge, we proposed an innovative subgrid cage structure design strategy: drawing inspiration from confinement engineering concepts in nanocages, molecular cages, and metal–organic frameworks, we constructed discrete structural units with permanent cavities within an inorganic lattice.[12] These subgrid cages create a unique energy-modulation environment—leveraging spatial confinement effects to precisely control ion separation and coordination fields, while utilizing their large-volume independent unit characteristics to optimize energy migration pathways.[13] In practical implementation, we designed subgrid cages with bilayer/multilevel structures within an inorganic host (Fig. 1), successfully synthesizing highly efficient NIR Cr^{3+}–Ln^{3+} co-doped luminescent materials. Within the $GdAl_{1.5}Ga_{1.5}(BO_3)_4$ host, Gd^{3+} ions reside within an inner cage formed by BO_3 tri-

[a]*Institute of Light+X Science and Technology, Faculty of Electrical Engineering and Computer Science, Ningbo University, Ningbo, 315211, P. R. China. E-mail: zsagdut2016@yeah.net, lychris@sina.com*
[b]*School of Biomedical Engineering, Guangzhou Medical University, Guangzhou, Guangdong, 511436, P. R. China*

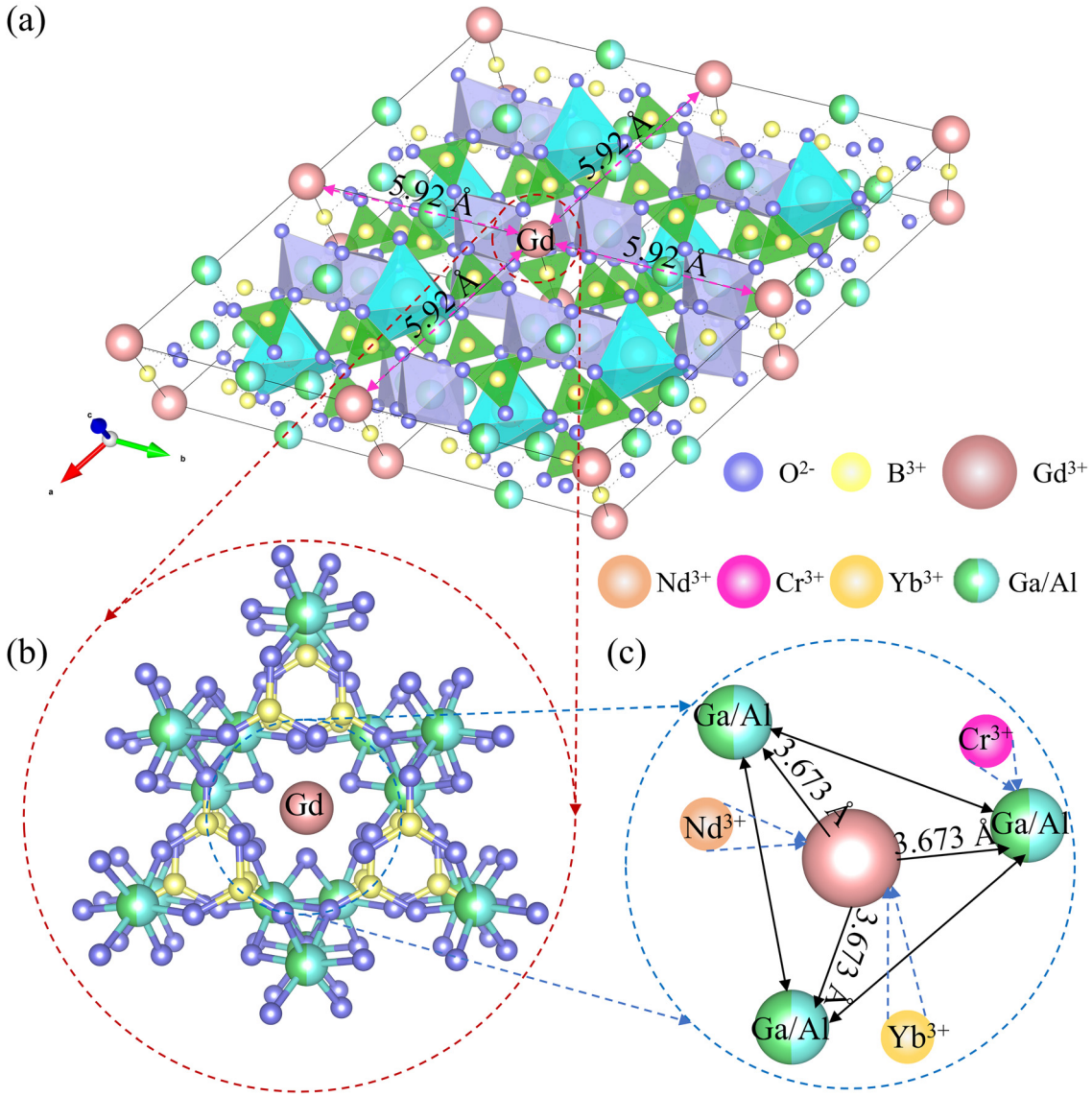

Fig. 1 (a) Three-dimensional crystallographic structure of $GdAl_{1.5}Ga(BO_3)_4$. (b) The double cage structure of the central Gd^{3+} ions consists of the Al/GaO_6 polyhedron along with the $[BO_3]$ polyhedron. (c) The local crystal structure of the central Gd^{3+} ions.

angular units, while AlO_6/GaO_6 octahedra constitute an outer cage.[14] When Cr^{3+}–Ln^{3+} ion pairs occupy Gd and Al/Ga sites, respectively, the separation between adjacent Gd^{3+} ions exceeds 5 Å, whereas the Cr^{3+}–Ln^{3+} pair distance is only 3.673 Å.[15] This bilayer cage structure not only suppresses energy migration between Ln^{3+} ions but also promotes highly efficient energy transfer between the sensitizer (Cr^{3+}) and the luminescent center (Ln^{3+}) within the cage.

Based on this strategy, $GdAl_{1.5}Ga_{1.5}(BO_3)_4:Cr^{3+},Ln^{3+}$ (Ln = Yb, Nd, Er) is established as a novel class of high-performance NIR phosphors. A key breakthrough is the achievement of highly efficient $Cr^{3+} \rightarrow Ln^{3+}$ energy transfer (η_{ETE}: 61% for Yb^{3+}; 82% for Nd^{3+}; 46% for Er^{3+}), with the Cr^{3+}–Yb^{3+} co-doped system exhibiting a PLQY of 86% while retaining 94% photoluminescence (PL) intensity at 423 K. The fabricated NIR phosphor-converted light-emitting diodes (pc-LEDs) demonstrate performance metrics meeting industrial application standards: the peak output power reaches 127 mW with a photoelectric conversion efficiency (PCE) of 13% under a 300 mA driving current, surpassing the comprehensive performance of existing Cr^{3+}-doped phosphor systems.

2. Experimental section

2.1. Sample synthesis

A series of compounds, denoted as GAGBO:$x$$Cr^{3+}$, GAGBO:$x$$Cr^{3+}$,$y$$Yb^{3+}$, GAGBO:$x$$Cr^{3+}$,$y$$Nd^{3+}$, and GAGBO:$x$$Cr^{3+}$,$y$$Er^{3+}$ (where GAGBO represents $GdAl_{1.5}Ga(BO_3)_4$), were synthesized

via a standard high-temperature solid-state reaction method. The starting materials comprised high-purity oxides: gadolinium oxide (Gd_2O_3, 99.99%), aluminum oxide (Al_2O_3, 99.99%), gallium oxide (Ga_2O_3, 99.99%), boron trioxide (B_2O_3, 99.95%), chromium(III) oxide (Cr_2O_3, 99.95%), ytterbium oxide (Yb_2O_3, 99.99%), neodymium oxide (Nd_2O_3, 99.99%), and erbium oxide (Er_2O_3, 99.99%).

Stoichiometric amounts of the precursors were accurately weighed, vigorously ground in an agate mortar to ensure homogeneous mixing, and then transferred into an alumina crucible. The mixture underwent a two-stage thermal treatment in a muffle furnace: first, preheating at 500 °C for 2 hours to eliminate volatile impurities and enhance precursor interactions, and subsequently, calcination at 1100 °C for 6 hours to achieve phase formation and crystallization. Following sintering, the samples were allowed to cool naturally to ambient temperature within the furnace before further characterization.

2.2. Characterization

The phase composition of the powder samples was characterized by powder X-ray diffraction using a Bruker D8 Advance diffractometer with Cu Kα_1 radiation (λ = 1.5406 Å) at 36 kV and 20 mA. Diffraction patterns were recorded across the 2θ range from 10° to 80°. X-ray photoelectron spectroscopy was conducted on a Thermo Scientific K-Alpha spectrometer (USA) to analyze elemental composition and chemical states. Optical properties were systematically investigated using a UV-Vis-NIR spectrophotometer (PerkinElmer Lambda 750) and an Edinburgh FLS1000 photoluminescence system equipped with a TAP-02 temperature-controlled cryostat (operating range: 77–300 K). Microstructural analysis was performed by scanning electron microscopy on a ZEISS Sigma 360 instrument (Germany) at an accelerating voltage of 30 kV.

The optoelectronic performance of the fabricated NIR pc-LED devices, including PCE and output power, was characterized using a HAAS 2000 photometric and electrical testing system.

2.3. NIR pc-LED device fabrication

The synthesized NIR phosphors—GAGBO:Cr^{3+}, GAGBO:Cr^{3+}, Yb^{3+}, and GAGBO:Cr^{3+},Nd^{3+}—were thoroughly mixed with silicone resins A and B (mass ratio A : B = 1 : 10) at a phosphor-to-silicone weight ratio of 1 : 2. The homogeneous mixture was dispensed onto 450 nm LED chips (nominal power: 10 W). The coated chips were then cured in a constant-temperature oven at 150 °C for 4 hours to complete the encapsulation.

3. Results and discussion

3.1. Analysis of the crystal structure and morphology

Fig. 2a presents the X-ray diffraction (XRD) patterns of $GdAl_{1.5}Ga_{1.5-x}(BO_3)_4$:$x$$Cr^{3+}$ phosphors at varying doping concentrations (x). All diffraction patterns exhibit excellent agreement with the reference PDF# 51-0584 (GAGBO), confirming the phase purity of the synthesized NIR phosphors. Fig. S1 shows the XRD patterns for GAGBO:0.15Cr^{3+},$y$$Yb^{3+}$ (y = 0.05, 0.12), GAGBO:0.15Cr^{3+},$y$$Nd^{3+}$ (y = 0.12, 0.15) and GAGBO:0.15Cr^{3+},$y$$Er^{3+}$ (y = 0.05, 0.12). All XRD patterns in Fig. S1 match well with PDF# 51-0584, indicating that Cr^{3+} and Ln^{3+} co-doping did not destroy the crystal structure of the $GdAl_{1.5}Ga_{1.5}(BO_3)_4$ host. To determine the valence state of Cr, X-ray photoelectron spectroscopy (XPS) analysis was performed. Fig. 2b shows the full survey scan, where the binding energies at 141.7 eV, 19.7 eV, 193.7 eV, 74.7 eV, 530.7 eV and 594.7 eV correspond to Gd-4d, Ga-3d, B-1s, Al-2p, O-1s, and Cr-2p, respectively.

Fig. 2c, d and Fig. S2 present detailed XPS spectra for Gd-4d, Ga-3d, B-1s, Al-2p, O-1s, and Cr-2p from the GAGBO:0.08Cr^{3+} phosphor. Notably, the Cr-2p spectrum reveals only the presence of Cr^{3+}, with no detectable signals corresponding to Cr^{4+} or Cr^{6+}, confirming that chromium exists exclusively in the trivalent state. Fig. 2e shows scanning electron micrographs (SEM) and energy-dispersive spectroscopy (EDS) analysis of the GAGBO:0.08Cr^{3+} phosphor. The polyhedral particles have a diameter of approximately 2–3 μm. Complementary elemental mapping by EDS performed on randomly selected particles further confirms the homogeneous spatial distribution of all constituent elements: Gd, Al, Ga, B, O, and Cr.

3.2. Photoluminescence properties

Fig. 3a presents the diffuse reflectance spectra of the undoped GAGBO, GAGBO:0.08Cr^{3+}, GAGBO:0.15Cr^{3+},0.12Yb^{3+} and GAGBO:0.15Cr^{3+},0.08Nd^{3+}. Notably, Cr^{3+} doping introduces two distinct absorption bands within the 350–800 nm range. These bands are assigned to the characteristic spin-allowed transitions of Cr^{3+}: the higher-energy band to the $^4A_2 \rightarrow {}^4T_1(^4F)$ transition and the lower-energy band to the $^4A_2 \rightarrow {}^4T_2(^4F)$ transition.[16,17] Notably, these characteristic absorption features persist in the spectra of Yb^{3+} and Nd^{3+} co-doped samples (Fig. S3). Strong absorption was observed in the 250–350 nm range, referred to as the Tauc region, which arises from valence-to-conduction band transitions.[18,19] The optical bandgap (E_{opt}) was determined using Tauc's relation:[20,21]

$$(\alpha h\nu)^2 = A(h\nu - E_{opt}) \quad (1)$$

Here, α is the absorption coefficient, approximated from the reflectance (R_∞) data using the Kubelka–Munk relation:[22]

$$\alpha \propto \frac{(1-R_\infty)^2}{2R_\infty} \quad (2)$$

Fig. S4 shows plots of $(\alpha h\nu)2$ *versus* photon energy ($h\nu$). Linear extrapolation of the absorption edge in this Tauc plot yields an estimated indirect optical bandgap of 4.10 eV. Fig. 3b shows the representative photoluminescence excitation (PLE) and PL spectra of the Cr^{3+}-doped phosphor. The PLE spectrum exhibits two distinct excitation bands: one in the 350–500 nm region and another in the 500–700 nm region. These two bands are attributed to the spin-allowed $^4A_2 \rightarrow {}^4T_1(^4F)$ and

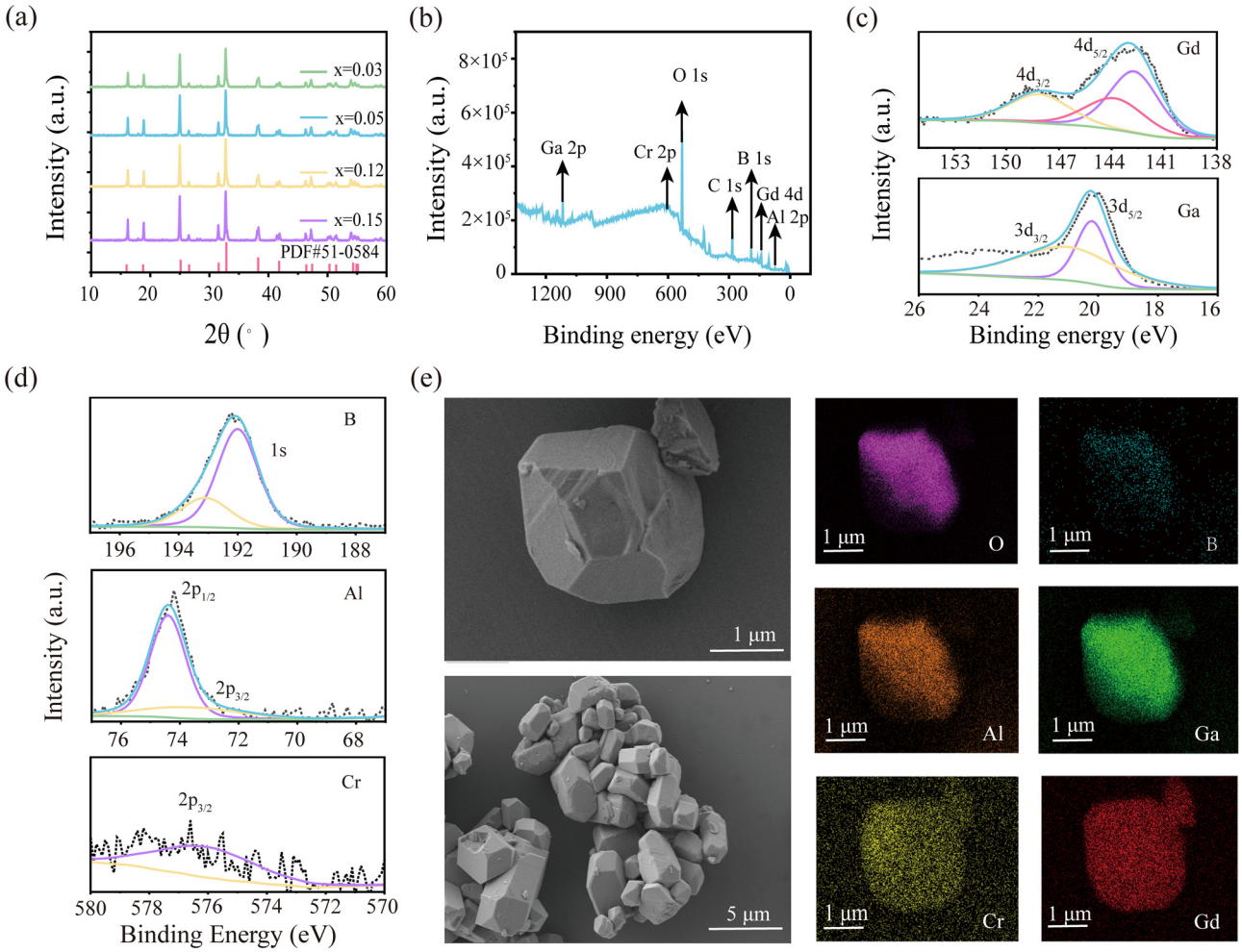

Fig. 2 (a) The XRD patterns of the GAGBO:xCr^{3+} (x = 0.03–0.15) phosphors. (b) The XPS spectra of GAGBO:0.08Cr^{3+}. (c and d) The detailed regions for Gd-4d, Ga-3d, B-1s, Al-2p and Cr-2p. (e) SEM images and EDS elemental mapping graphs of GAGBO:0.08Cr^{3+}.

$^4A_2 \rightarrow {}^4T_2(^4F)$ transitions of Cr^{3+}, respectively.[23] Upon excitation at 425 nm, a broad NIR emission band centered at 766 nm is observed. This emission originates from the radiative $^4T_2(^4F) \rightarrow {}^4A_2$ transition of Cr^{3+}. The agreement between these excitation bands and the absorption features in the diffuse reflectance spectra (Fig. 3a) confirms Cr^{3+} as an effective NIR luminescent center in this GAGBO host.

To investigate the concentration dependence of the Cr^{3+} NIR luminescence, a series of Cr^{3+}-doped phosphors with varying Cr^{3+} concentrations were synthesized. Fig. 3c presents their concentration-dependent PL spectra recorded under identical excitation conditions. Irrespective of the doping level, all samples exhibit a single, broad emission band peaking at 766 nm. Notably, GAGBO:0.08Cr^{3+} shows extensive NIR emission with a full width at half maximum of 123 nm (Fig. 3b), which is in agreement with the emission of commercial blue LEDs.[24] The PL intensity increases with rising Cr^{3+} concentration, reaching a maximum at the optimal concentration of x = 0.08. Further increases in x beyond this doping concentration lead to a gradual decline due to concentration quenching of Cr^{3+}. This quenching is attributed to enhanced non-radiative energy transfer between neighboring Cr^{3+} ions at higher doping concentrations.[25,26]

Thermal stability is a critical performance parameter for Cr^{3+}-doped phosphors in solid-state lighting, particularly given that operational temperatures of LED chips can reach 423 K (150 °C)—a regime where thermal quenching typically degrades emission.[27] Fig. 3d presents the temperature-dependent PL intensity of the optimized GAGBO:0.08Cr^{3+} phosphor. The integrated emission intensity gradually decreases with increasing temperature due to thermal quenching. Significantly, at 423 K (150 °C), the PL intensity retains 93% of its room-temperature value, demonstrating the exceptional thermal stability of GAGBO:0.08Cr^{3+} phosphors. The inset of Fig. 3d illustrates the underlying thermal quenching mechanism. Following excitation by blue light, electrons are promoted from the $^4A_2$ ground state to higher-energy configurations: $^4T_1$ (^4P), $^4T_1$ (^4F), or $^4T_2$ (^4F). These excited states undergo rapid non-radiative relaxation to the lowest excited state, $^4T_2$ (^4F). Radiative decay from this state to the $^4A_2$ ground

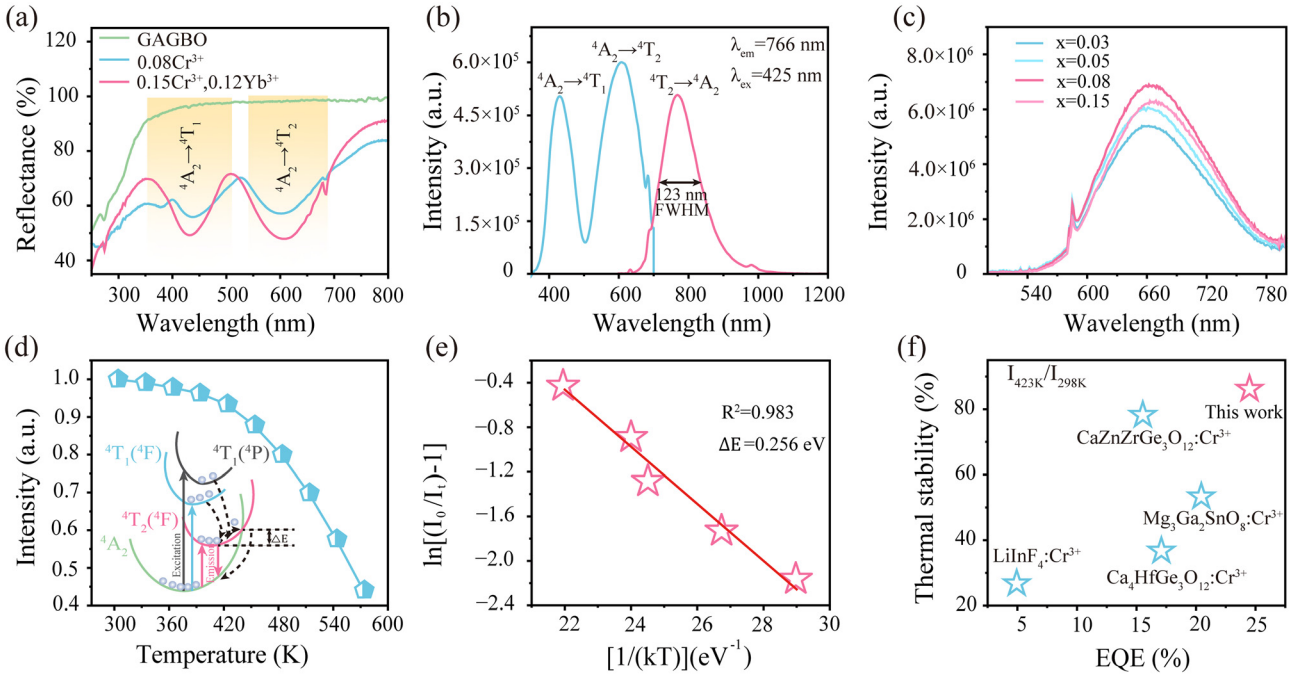

Fig. 3 (a) Diffuse reflectance spectra of GAGBO, GAGBO:0.08Cr^{3+}, and GAGBO:0.15Cr^{3+},0.12Yb^{3+}. (b) PLE and PL spectra of GAGBO:0.08Cr^{3+}. (c) PL spectra of GAGBO:xCr^{3+} (x = 0.03–0.15) upon 425 nm blue light excitation. (d) Temperature-dependent normalized integrated PL intensities of GAGBO:0.08Cr^{3+}; the inset photo shows the luminescence temperature quenching schematic of Cr^{3+} ions in GAGBO:0.08Cr^{3+}. (e) Fitting line of ln [(I_0/I_t) − 1] *vs.* [1/(kT)]. (f) Comparison of thermal stability and external quantum efficiency between Cr^{3+}-doped phosphors and GAGBO:0.08Cr^{3+}.

state generates the observed NIR emission.[28] At elevated temperatures, however, electrons in the $^4T_2$ (^4F) state gain sufficient thermal energy to reach the crossing point between the excited-state and ground-state potential energy surfaces. This enables non-radiative deactivation to the ground state.[29] The energy barrier (ΔE) for this crossover fundamentally governs thermal stability: a larger ΔE impedes thermal population of the crossing point, thereby favoring radiative emission and enhancing thermal stability.[30,31]

To quantitatively evaluate this effect, we calculated the activation energy ΔE using the Arrhenius equation:[32–34]

$$I(T) = \frac{I_0}{1 + A_{\exp}(-\Delta E/kT)} \quad (3)$$

As shown in Fig. 3e, the fitted ΔE value for GAGBO:0.08Cr^{3+} is calculated to be 0.256 eV. This high activation energy directly correlates with the observed superior thermal stability (93%@423 K) and the measured external quantum efficiency of 24%. As demonstrated in Fig. 3f, this performance surpasses the reported Cr^{3+}-doped phosphors.

3.3. Energy transfer of Cr^{3+}–RE^{3+} co-doping

To investigate energy transfer (ET) from Cr^{3+} to Ln^{3+} (Ln^{3+} = Yb, Nd and Er) in the GAGBO host, the PLE spectra were monitored at the characteristic emission wavelengths of Ln^{3+}: 983 nm for Yb^{3+}, 1063 nm for Nd^{3+}, and 766 nm for Er^{3+} (Fig. 4a, c and Fig. S5). These PLE spectra showed two broad excitation bands attributed to the spin-allowed $^4A_2 \rightarrow {}^4T_1(^4P)$ and $^4A_2 \rightarrow {}^4T_2(^4F)$ transitions of Cr^{3+}. When monitoring the Ln^{3+} emission, these Cr^{3+} excitation bands confirm the occurrence of energy transfer from Cr^{3+} to Ln^{3+}. Concentration-dependent PL spectra reveal that the PL intensity of Ln^{3+} reaches a maximum at y = 0.12 for Yb^{3+} (Fig. 4b), 0.08 for Nd^{3+} (Fig. 4e) and 0.005 for Er^{3+} (Fig. S5). Notably, beyond these critical values, the PL intensity of Ln^{3+} decreases with further increase in the Ln^{3+} doping concentration due to concentration quenching. Upon excitation at 425 nm, the decay lifetimes of Cr^{3+} decrease with increasing Ln^{3+} concentration (Fig. S6). The reduction in Cr^{3+} decay lifetimes, as shown in Fig. 4c, d and Fig. S6, provides direct evidence for efficient ET from Cr^{3+} to Ln^{3+}. Collectively, the observation of Cr^{3+} excitation bands in the Ln^{3+}-monitored PLE spectra, the concentration dependence of Ln^{3+} PL intensity, and the corresponding decrease in the Cr^{3+} decay lifetime provide direct evidence for efficient energy transfer from Cr^{3+} to Ln^{3+} ions.

To quantify the η_{ETE} of Cr^{3+}–Ln^{3+}, decay curves of Cr^{3+} emission were measured in GAGBO as a function of Ln^{3+} doping concentration. The average lifetimes (τ_{ave}) were calculated using the following formula, with the results presented in Fig. 4c and f:[35,36]

$$\tau_{ave} = \frac{\int_0^\infty tI(t)\mathrm{d}t}{\int_0^\infty I(t)\mathrm{d}t} \quad (4)$$

These decay dynamics further confirm the occurrence and efficiency of the energy transfer processes.[34] The results reveal a significant decrease in the average decay lifetime of Cr^{3+} ions

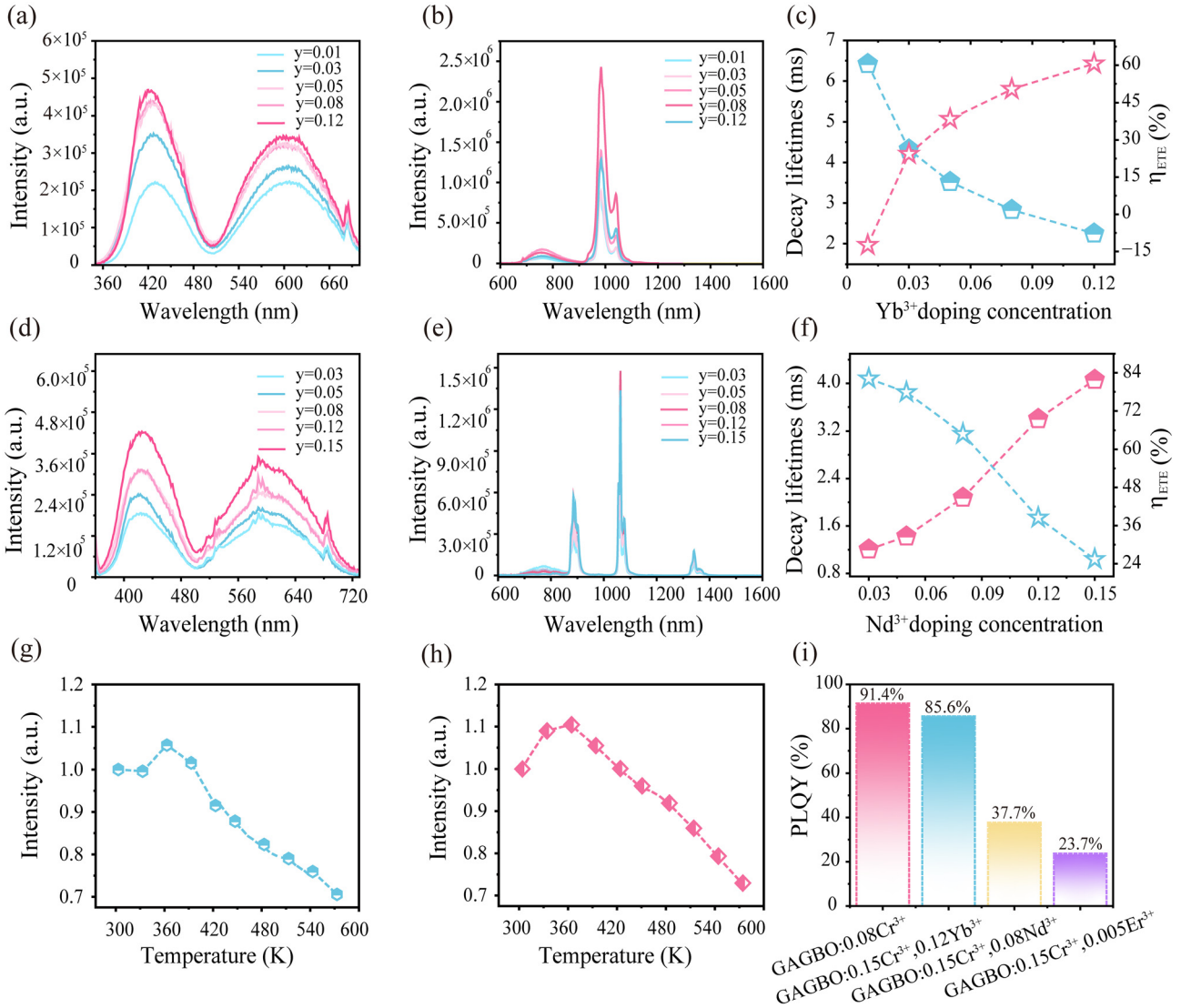

Fig. 4 The (a) excitation spectra and (b) emission spectra of GAGBO:0.15Cr^{3+},yYb^{3+} (*y* = 0.01–0.12). (c) Decay lifetimes and energy transfer efficiency (η_{ETE}) dependent on the Yb^{3+} doping concentration. The (d) excitation spectra and (e) emission spectra of GAGBO:0.15Cr^{3+},yNd^{3+} (*y* = 0.03–0.15). (f) Decay lifetimes and η_{ETE} dependent on the Nd^{3+} doping concentration. The normalized integrated emission intensity diagram of (g) GAGBO:0.15Cr^{3+},0.12Yb^{3+} and (h) GAGBO:0.15Cr^{3+},0.08Nd^{3+}. (i) PLQY measurement of GAGBO:0.15Cr^{3+},0.12Yb^{3+} and GAGBO:0.15Cr^{3+},0.08Nd^{3+}.

with increasing Ln^{3+} concentration. For Yb^{3+} co-doping, τ_{ave} decreased from 6.42 ms to 2.25 ms. Similarly, for Nd^{3+} co-doping, τ_{ave} decreased from 4.08 ms to 1.04 ms. A parallel trend was observed in the Cr^{3+}–Er^{3+} co-doped system (Fig. S6). The η_{ETE} from Cr^{3+} (sensitizer) to Yb^{3+} or Nd^{3+} (activator) can be estimated using the following equation:[37,38]

$$\eta_{ETE} \approx 1 - \frac{\tau_s}{\tau_{s0}} \quad (5)$$

where τ_s and τ_{s0} represent the decay lifetimes of Cr^{3+} in the presence and absence of the acceptor ion (Ln^{3+}). Fig. 4c and f show that the η_{ETE} increases with rising Ln^{3+} content, indicating enhanced energy transfer. Notably, the maximum η_{ETE} values were 61%, 82% and 46% for the $Cr^{3+} \rightarrow Yb^{3+}$, Nd^{3+} and Er^{3+} (Fig. S7) pairs, respectively.

Long-term operation of pc-LEDs can elevate the temperature of the LED chip to 423 K or higher. Consequently, the working temperature of the LED chip is a critical factor influencing phosphor utilization efficiency. Temperature-dependent PL spectra of Cr^{3+}–Ln^{3+} co-doped samples were measured across a temperature gradient (303–573 K) to evaluate thermal stability. As shown in Fig. 4g, h and Fig. S8, the normalized integral emission intensity of all samples gradually decreases with increasing temperature. Notably, the Cr^{3+}-doped sample exhibits significantly more pronounced thermal quenching. This substantial intensity reduction is attributed to thermally activated non-radiative relaxation pathways dominating at higher temperatures.[39]

In contrast, co-doping with Yb^{3+}, Nd^{3+} or Er^{3+} ions substantially improves thermal stability. This enhancement stems from two key factors:[40] firstly, the energy transfer efficiency from Cr^{3+} to Ln^{3+} increases at elevated temperatures, allowing Cr^{3+} to transfer a larger fraction of its absorbed energy before the occurrence of non-radiative losses, thereby mitigating thermal quenching within the Cr^{3+} system itself;[41–43] secondly, the characteristic NIR emissions of Ln^{3+} demonstrate excellent intrinsic thermal stability. Quantitatively, 94% and 100% of the normalized emission intensities are retained at 423 K for the Yb^{3+} and Nd^{3+} co-doped samples, respectively. This synergistic effect leads to superior overall thermal performance for the co-doped phosphors. A similar improvement in thermal stability is observed upon introducing Er^{3+} ions, as detailed in Fig. S9. Furthermore, Cr^{3+}–Ln^{3+} co-doping yielded internal quantum efficiency (IQE) values of 86% for Cr^{3+}–Yb^{3+}, 38% for Cr^{3+}–Nd^{3+}, and 24% for Cr^{3+}–Er^{3+}, respectively. The combination of exceptionally high IQE and excellent thermal stabilities for the Cr^{3+}–Ln^{3+} co-doped phosphors highlights their potential as promising candidate phosphors for high-performance NIR pc-LEDs.

3.4. Luminescence performance and applications

To evaluate the practical application potential of GAGBO:Cr^{3+} and GAGBO:Cr^{3+}–Ln^{3+} phosphors, NIR pc-LEDs were fabricated by coating these four types of phosphors onto 450 nm blue light chips. When the driving current increases from 10 mA to 300 mA, the electroluminescence (EL) intensity gradually increases, as shown in Fig. 5a and d. From Fig. 5b, c, e and f, the output power of the NIR pc-LED chip increases

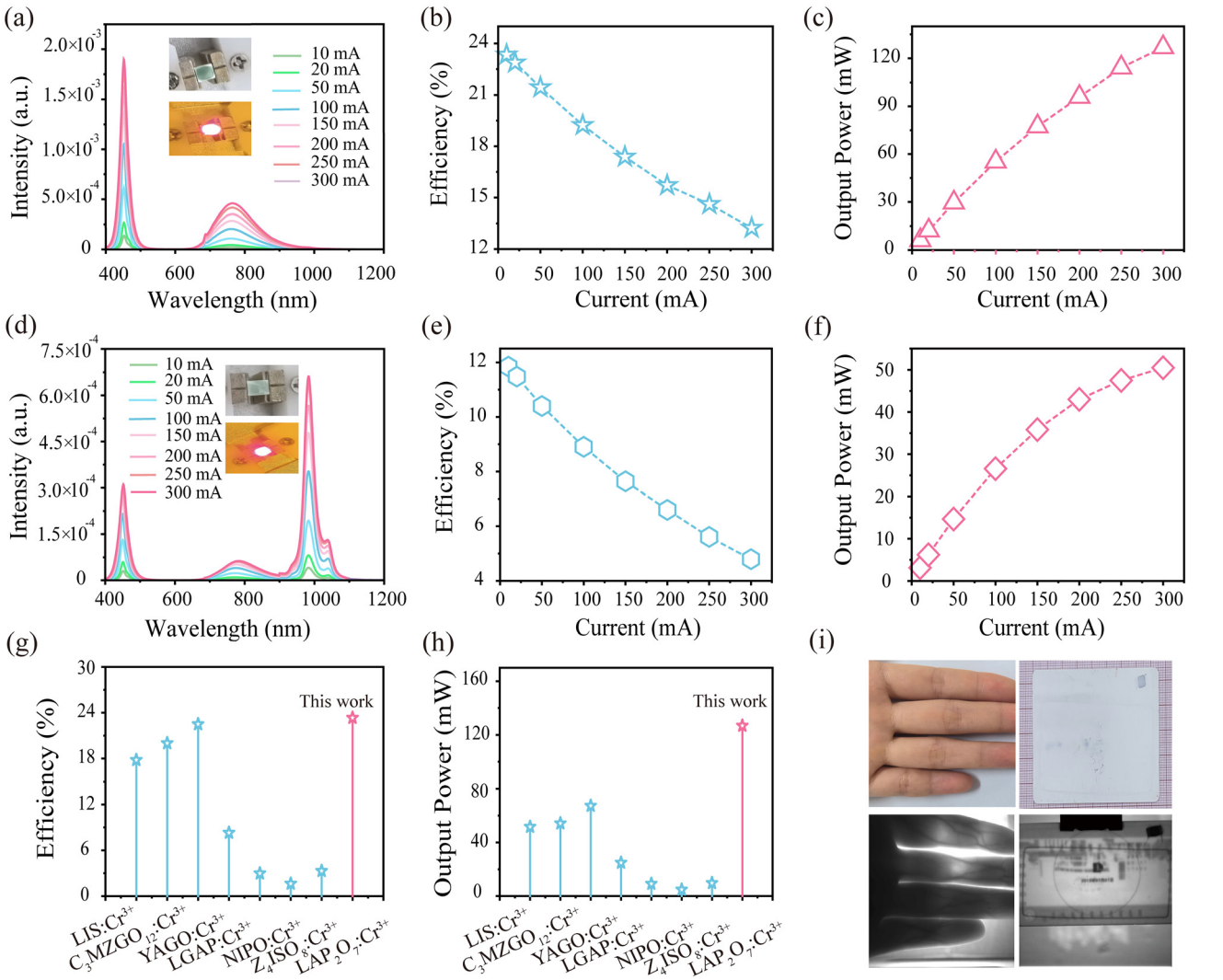

Fig. 5 The (a) emission spectra, (b) photoelectric conversion efficiency (PCE) and (c) output power of GAGBO:0.08Cr^{3+} phosphor-based NIR pc-LEDs; the inset shows a photograph of the LED device. The (d) emission spectra, (e) PCE and (f) output power of GAGBO:0.15Cr^{3+},0.12Yb^{3+} phosphor-based NIR pc-LEDs; the inset shows a photograph of the LED device. Comparison of (g) PCE at 10 mA and (h) output power at 300 mA for the Cr^{3+} phosphor-based NIR pc-LEDs. (i) NIR images of a female palm's veins and a campus ID card, illuminated by visible light and custom-built pc-LEDs.

with the current, while the photonic conversion efficiency gradually decreases. At a driving current of 300 mA, the output powers of the GAGBO:Cr^{3+} and GAGBO:Cr^{3+}–Ln^{3+} pc-LED chips reach 127 mW, 51 mW, 10 mW, and 12 mW. The photonic conversion efficiencies of the GAGBO:Cr^{3+} and GAGBO:Cr^{3+},Yb^{3+} pc-LED chips are 13% and 4.8%, respectively. Compared to the PCE at 10 mA and output power of NIR pc-LEDs at 300 mA reported previously (Tables S1 and S4), GAGBO:Cr^{3+} and GAGBO:Cr^{3+},Yb^{3+} pc-LEDs exhibit superior performance (Fig. 5g and h), demonstrating their versatile potential.

Considering the excellent luminescence properties of these phosphors, the practical applications of GAGBO:Cr^{3+}, GAGBO:Cr^{3+}–Ln^{3+} were investigated. The 10 W high-power LED chips fabricated with the NIR phosphor samples prepared in this study highlight their significant potential for non-destructive testing and human vein imaging and recognition. The fabricated LED chips served as NIR light sources to capture images of a plastic campus card and a human hand under complete darkness. The captured scenes and effects are shown in Fig. 5i. When photographed with a regular digital camera under visible light, the external features of the object were visible. However, nothing was visible when the visible light source was turned off and the photo was taken using the same digital camera. In contrast, when only the NIR light source was activated and photographed with an NIR camera, a clear image of the card (including the integrated circuit structure) and the veins and bones of the hand could be observed. The NIR light source demonstrates excellent night vision capabilities, non-destructive testing abilities, and effective tissue penetration for human body imaging.

4. Conclusion

This work demonstrates a subgrid-cage confinement strategy to overcome the fundamental challenge of uncontrollable energy migration in Cr^{3+}–Ln^{3+} phosphors. The discrete bilayer cage structure within $GdAl_{1.5}Ga_{1.5}(BO_3)_4$ enables precise localization of Cr^{3+} (octahedral sites) and Ln^{3+} (dodecahedral sites), constraining their separation to the optimal 3.673 Å. This architecture achieves ultra-broadband NIR emission (650–1600 nm), fully spanning all biological transparency windows, through highly efficient $Cr^{3+} \rightarrow Ln^{3+}$ energy transfer (η_{ETE}: 61% for Yb^{3+}, 82% for Nd^{3+}, and 46% for Er^{3+}). Crucially, the strategy simultaneously suppresses detrimental Ln^{3+} migration and maximizes sensitizer–activator interaction, yielding record performance: a PLQY of 86% for Cr^{3+}–Yb^{3+} and exceptional thermal stability (94%@423 K). The fabricated NIR pc-LEDs deliver industry-leading output power (127 mW) and photoelectric efficiency (13%) under a 300 mA driving current, enabling high-contrast biological imaging applications. This subgrid-cage confinement paradigm provides a universal solution for overcoming the quantum efficiency bottleneck in next-generation broadband NIR phosphors.

Author contributions

Yang Li conceived the idea, designed the experiment, and analyzed the data. Simeng Cao provided samples for all measurements and collected all data. Ximei An, Lei Yang, Mengting Gao, Zhiyue Yang, Chao He and Zonglong Guo carried out device-fabricated characterization. Yang Li, Shaoan Zhang and Simeng Cao contributed to the technical discussions of results. Simeng Cao wrote the manuscript. Shaoan Zhang and Yang Li improved the manuscript and directed and supervised the project. All authors discussed and commented on the manuscript.

Conflicts of interest

There are no conflicts to declare.

Data availability

The authors confirm that the data supporting the findings of this study are available within the article. Supplementary information is available. See DOI: **https://doi.org/10.1039/d5qi01468a**.

Acknowledgements

This work was financially supported by the National Natural Science Foundation of China (Grant No. 52402192 and 52172083), the Zhejiang Province Key R&D Program: Vanguard and Leading Geese Projects (Grant No. 2024C01190), the Guangzhou Key Research and Development Program (Grant No. 2023B03J1239), and the Program for Innovative Research Team in University of Education System of Guangzhou (Grant No. 202235404). This work was also financially supported by the Guangdong Basic and Applied Basic Research Foundation (Grant No. 2022A1515110463).

References

1 D. Gao, B. Chen, X. Sha, Y. Zhang, X. Chen, L. Wang, X. Zhang, J. Zhang, Y. Cao, Y. Wang, L. Li, X. Li, S. Xu, H. Yu and L. Cheng, Near Infrared Emissions from Both High Efficient Quantum Cutting (173%) and Nearly-Pure-Color Upconversion in $NaY(WO_4)_2$:Er^{3+}/Yb^{3+} with Thermal Management Capability for Silicon-Based Solar Cells, *Light: Sci. Appl.*, 2024, **13**, 17.

2 D. Liu, G. Li, P. Dang, Q. Zhang, Y. Wei, L. Qiu, H. Lian, M. Shang and J. Lin, Valence Conversion and Site Reconstruction in Near-Infrared-Emitting Chromium-Activated Garnet for Simultaneous Enhancement of Quantum Efficiency and Thermal Stability, *Light:Sci. Appl.*, 2023, **12**, 248.

3 W. Liu, W. Deng, W. Wang, H. Wu, C. Gao, Y. Xie, J. Zhao, X. Dong, Z. Zhao, Z. Zheng, Y. Chi, L. Duan, X. Zhan, Y. Zou, H. Wu, J. Peng and Y. Cao, Ultrahigh-Radiance Near-Infrared Organic Light-Emitting Diodes, *Nat. Photonics*, 2025, **19**, 650–657.

4 Y. Xie, W. Liu, W. Deng, H. Wu, W. Wang, Y. Si, X. Zhan, C. Gao, X.-K. Chen, H. Wu, J. Peng and Y. Cao, Bright Short-Wavelength Infrared Organic Light-Emitting Devices, *Nat. Photonics*, 2022, **16**, 752–761.

5 Y. Zhang, S. Miao, Y. Liang, C. Liang, D. Chen, X. Shan, K. Sun and X.-J. Wang, Blue LED-Pumped Intense Short-Wave Infrared Luminescence Based on Cr^{3+}-Yb^{3+}-Co-Doped Phosphors, *Light: Sci. Appl.*, 2022, **11**, 650.

6 M. Zhang, P. Dang, Y. Wan, Y. Wang, Z. Zeng, D. Liu, Q. Zhang, G. Li and J. Lin, Tailoring Ultra–Wide Visible–NIR Luminescence by Ce^{3+}/Cr^{3+}/Yb^{3+}–Alloying Sc–Based Oxides for Multifunctional Optical Applications, *Adv. Opt. Mater.*, 2024, **12**, 2302941.

7 Y. Wang, M. Shang, Y. Sun, Y. Zhu, X. Xing, P. Dang and J. Lin, Small Stokes Shift and Two–Site Occupation in the ANB_2O_6:Cr^{3+} (A = Zn/Mg) Phosphors Toward Highly Efficient Ultra–Broadband Near–Infrared Emission for Multifunctional Applications, *Adv. Opt. Mater.*, 2024, **12**, 2302611.

8 Z. Yang, G. Lu, J. Ma, T. Yang, G. Xiang, L. Li, X. Zhou and Z. Xia, Non–Stoichiometric Calcium Addition in Red–Emitting $CaSc_2O_4$:Eu^{2+} Phosphor toward Enhanced Photoluminescence Quantum Efficiency for LED Applications, *Laser Photonics Rev.*, 2025, 2500300.

9 D. Duan, S. Yu, Y. Wu, Y. Dong, Q. Shao and J. Jiang, Cr^{3+}–Doped Far–Red Phosphors with Zero Thermal Quenching and Excellent Spectral Matching for Plant Lighting Application, *J. Am. Ceram. Soc.*, 2024, **107**, 6070–6079.

10 S. Zhang, S. Qin, Y. Xiao, Z. Liu, X. Hu, Z. Xiao, D. Huang, L. Han and X. Ye, Near-Infrared Luminescent Materials: A Review of Their Practical Applications and Prospective Advancements, *Dalton Trans.*, 2025, **54**, 6717–6740.

11 X. Zhang, D. Sun, P. Luo, L. Zhou, Z. Lu, J. Liu, C. Fan, X. Ye and H. You, Tunable Luminescence via Cr^{3+}-Yb^{3+}/Nd^{3+} Energy Transfer in Cr^{3+} and Yb^{3+}/Nd^{3+} Coactivated NIR Phosphors for Non-Destructive Analysis, *Inorg. Chem. Front.*, 2024, **11**, 8679–8689.

12 N. Rakov, F. Matias and G. S. Maciel, Temperature Sensing Performance of Er^{3+}:Yb^{3+} Co-Doped CaF_2 Ceramic Powders Using Near-Infrared Light, *J. Rare Earths*, 2025, **43**, 253–261.

13 J. Wang, C. Gong, S. Yang, Q. Zhu, X. Wang and J. G. Li, Cr^{3+} Activated $Na_3RESi_3O_9$ (RE = Y, Lu, Sc) Silicate Broadband Near-Infrared Phosphors for Luminescence towards NIR-II Region via a Multi-Site Occupancy Strategy, *J. Rare Earths*, 2024, **42**, 1447–1457.

14 R. Shi, S. Miao, X. Lv, D. Chen, Y. Zhang and Y. Liang, High–Efficiency Short–Wave Infrared Emitter Enabled by Cr^{3+}-Yb^{3+} Co–Doped Phosphor, *Adv. Opt. Mater.*, 2024, **12**, 2303221.

15 X. Xie, W. Ge, Q. Zhang, Y. Tian, Z. Luo, S. Shang, J. Liu and W. Cao, A Novel Multifunctional and Broadband Near–Infrared Phosphor, $Lu_3MgGa_3GeO_{12}$:Cr^{3+}, Yb^{3+}, Nd^{3+} Achieved through a Chemical Unit Substitution and Energy Transfer Strategy, *Adv. Opt. Mater.*, 2025, **13**, 2401957.

16 X. Liu, L. Chen, X. Huo, F. Liu, C. Liao, L. Zhang, J. Zhang, S. Zhang, Y. Li, X. Wang and Y. Liu, From Two–Step Excitation to Persistent Luminescence: Revisiting $ZnGa_2O_4$:Cr^{3+} Phosphor Through Upconversion Charging Approach, *Adv. Opt. Mater.*, 2024, **12**, 2303018.

17 D. Liu, G. Li, P. Dang, Q. Zhang, Y. Wei, H. Lian, M. Shang, C. C. Lin and J. Lin, Simultaneous Broadening and Enhancement of Cr^{3+}Photoluminescence in $LiIn_2SbO_6$ by Chemical Unit Cosubstitution: Night–Vision and Near–Infrared Spectroscopy Detection Applications, *Angew. Chem., Int. Ed.*, 2021, **60**, 14644–14649.

18 W. Zhang, W. Wei, D. Liu, J. Lin and L. Wang, A Novel High-Efficient NIR Emitting Phosphor $Ca_2YAl_3Ge_2O_{12}$:Cr^{3+} Enabled by Chemical Unit Co-Substitution, *Ceram. Int.*, 2024, **50**, 41196–41206.

19 C. Dou, C. Cai, Z. Song and Q. Liu, Highly Quantum Efficient and Thermally Stable Near–Infrared–Emitting K–β–Al_2O_3:Cr^{3+} Phosphor, *Adv. Opt. Mater.*, 2024, **12**, 2301579.

20 Z. Chen, S. Zhang, Z. Li, H. Ye, H. Yan, J. Xu, L. Gao, Y. Li and S. Zhang, Thermally Stable NIR Broad Emission of Cr^{3+} Doping Phosphor with a High Output Power, *Inorg. Chem. Front.*, 2024, **11**, 6898–6908.

21 J. Klein, L. Kampermann, B. Mockenhaupt, M. Behrens, J. Strunk and G. Bacher, Limitations of the Tauc Plot Method, *Adv. Funct. Mater.*, 2023, **33**, 2304523.

22 Y. Zhuo, Y. Niu, F. Wu, Y. Wang, Q. Zhang, Y. Teng, X. Xie, H. Dong and Z. Mu, Super-wide-range tunable emission across NIR-II and NIR-III achieved by B-site cation co-substitution in Ni^{2+}-doped double perovskites for NIR light sources, *J. Mater. Chem. C*, 2025, **13**, 10621.

23 X. Xing, S. Huang, Y. Wang, L. Yu, Y. Sun and M. Shang, Highly Efficient Broadband Near-Infrared Luminescence Phosphors $Ca_3MgSn_{0.5}Zr_{0.5}Ge_3O_{12}$:$Pr^{3+}$,$Cr^{3+}$ for Multifunctional Applications in Pc-LEDs Field, *J. Rare Earths*, 2025, **43**, 1110–1119.

24 Q. Zhang, R. Sun, Q. Ni, J. Zhou, J. Li, H. Ni and J. Huo, Obtaining Versatile Cr^{3+}-Activated Phosphors with Improved Far-Red Emissions via Host Composition Modulation, *J. Rare Earths*, 2025, **43**, 874–881.

25 Z. Song, P. A. Tanner and Q. Liu, Host Dependency of Boundary between Strong and Weak Crystal Field Strength of Cr^{3+} Luminescence, *J. Phys. Chem. Lett.*, 2024, **15**, 2319–2324.

26 S. Zhang, Y. Long, P. Zhang, Z. Fang, Z. Li, H. Ye, G. Zheng, H. Jia, J. Qiu and Y. Li, Ultra-Transparent β-Ga_2O_3:Cr^{3+} Glass-Ceramics Enabling High-Efficiency True-Transmission Near-Infrared Light-Emitting Diodes, *J. Adv. Ceram.*, 2025, **14**, 9221075.

27 G. Liu, Z. Xiong, W. Chen, S. Zhang, Y. Wang and Z. Xia, $MgAl_2O_4$:Cr^{3+} Translucent Ceramics with Tunable

Broadband Near–Infrared Luminescence for Laser–Driven Light Source Detection, *InfoMat*, 2025, e70020.

28 F. Fan, S. Yu, Y. Li, Y. Xu, Y. Song, Y. Yan, H. Wu, W. Wang and L. Zhao, Enhancement of the NIR Emission of Cr^{3+}-Yb^{3+} Co-Doped $La_3GaGe_5O_{16}$ Phosphors by Doping Nd^{3+} Ions via Efficient Energy Transfer for NIR Spectroscopy Regulation, *Inorg. Chem.*, 2022, **61**, 13618–13626.

29 V. T. T. Le, D. M. Tien, V. X. Dao, T. Nguyen and H. T. Phan, Novel Rare-Earth-Free Far-Red-Emitting Phosphor Cr^{3+}, Al^{3+} Co-Doped Zn_2SnO_4 Toward Controlled Plant Flowering, *J. Electron. Mater.*, 2025, **54**, 3001–3013.

30 J. J. Schuyt, G. V. M. Williams and S. V. Chong, Cryogenic Charging and Discharging Kinetics of a Photostimulable Phosphor: Low Charge Rates at Low Temperatures, *J. Phys. Chem. Lett.*, 2025, **16**, 4828–4834.

31 D. R. Taikar, K. Sonkusare, S. J. Dhoble and R. S. Yadav, Recent Progress in Cr^{3+} Doped Phosphors for Indoor Plant Cultivation LEDs: A review, *J. Mol. Struct.*, 2025, **1331**, 141564.

32 Y. Fan, H. Wu, Y. Jin, Y. Li and Y. Hu, Ultra-Broadband Near Infrared Phosphor with Wide Spectral Range and Long Peak Wavelength Achieved by Double-Site Occupation, *J. Lumin.*, 2025, **283**, 121262.

33 Y. Yang, W. Lü, X. Kang, Z. Zhu, Q. Pan and Q. Zeng, Broadening Near-Infrared Emission and Enhancing Thermal Stability of Cr^{3+}-Activated $SrLaGa_3O_7$ Phosphors via Yb^{3+} Co-Doping, *J. Lumin.*, 2025, **280**, 121098.

34 S. Guo, C. Tang, L. Ma, R. Wei, X. Tian, F. Hu and H. Guo, Enhanced Broadband Near-Infrared Luminescence in Cr^{3+}-Activated $Gd_2Ga_{1-2x}Zn_xSi_xSbO_7$ Phosphors for Multifunctional Applications, *J. Lumin.*, 2025, **286**, 121356.

35 X. Liang, Y. Chen, T. Ouyang, F. Wu, Q. Zhang, Y. Teng, X. Xie, H. Xie, H. Dong and Z. Mu, Achieving enhanced, tunable and broadened NIR-II emission in Ni^{2+} doped $Li_2Mg_3TiO_6$ via cationic substitution strategy, *J. Photochem. Photobiol., A*, 2026, **470**, 116605.

36 S. Song, Z. Lu, Y. Yang, L. Shen, L. Liu, J. Huang, C. Zhou, L. Zhou and P. Chen, Integrated "All-In-One" Strategy toward Boosting Photoluminescence Performance in Cr^{3+}-Activated Ganet Phosphors, *J. Lumin.*, 2025, **281**, 121179.

37 H. Zhu, Y. Li, Y. Xi, C. Xin, C. Zhou, Z. Yang, L. Ruan, Y. Li, Y. Peng, M. S. Molokeev, A. Zolotov, J. Wang, Z. Zhou and M. Xia, Abnormal Lattice Shrinkage, Site Occupation, and Luminescent Properties of Cr^{3+}–Activated β–Al_2O_3 Structure Phosphors, *Laser Photonics Rev.*, 2025, **19**, 2401089.

38 Y. Niu, F. Wu, Y. Zhou, J. Li, Q. Zhang, Y. Teng, X. Xie, H. Dong and Z. Mu, Luminescence properties and applications of Ca_2ScTaO_6: Bi^{3+}, Ln^{3+} (Ln = Eu, Sm, Dy, Tb) phosphors, *Ceram. Int.*, 2025, **51**, 30597.

39 S. Zhang, Z. Li, H. Ye, X. An, J. Xu, Z. Chen, Y. Chen, Z. Fang, S. Sun, J. Qiu and Y. Li, Data Mining Evoking Scintillators Auto–Discovery for Low–LoD High–Resolution Deep–Penetrating X–Ray Imaging of Portable Digital Radiography, *Adv. Funct. Mater.*, 2025, **35**, 2415220.

40 L. Zhang, D. Wang, F. Liu, H. Wu, G. Pan, H. Wu, Z. Hao, H. Zhang and J. Zhang, Minimizing Bond Angle Distortion to Improve Thermal Stability of Cr^{3+} Doped Near–Infrared Phosphor, *Laser Photonics Rev.*, 2023, **17**, 2300092.

41 S. Cong, H. Yu, X. Gao, Z. Han, B. Chen, J. Sun and X. Li, Near-Infrared Emission Properties and LED Applications of $Y_2Ti_2O_7$:Cr^{3+}/Nd^{3+} Phosphors Improved by Doping with Ce^{3+} Ions, *Russ. J. Phys. Chem. A*, 2024, **98**, 2390–2399.

42 Z. Han, H. Yu, S. Cong, T. Liu, J. Sun, X. Li and B. Chen, Wide Near-Infrared II Emissions and LED Application of $Y_2Ti_2O_7$: Cr^{3+}/Yb^{3+}/Nd^{3+} Phosphors, *Appl. Phys. A: Mater. Sci. Process.*, 2023, **129**, 764.

43 Q. Zhu, Y. Sun, Y. Wang and Z. Xia, Flexible Composite Fluorescent Optical Fiber Sensor Embedded with Li_2HfO_3: Er^{3+}/Yb^{3+} for Physiological Temperature Monitoring, *Laser Photonics Rev.*, 2025, **19**, 2402225.

